Journal of Materials Chemistry A

Fe-Ni Foams Self-Heal during Redox Cycling via Reversible Formation/Homogenization of a Ductile Ni Scaffold

Journal:	*Journal of Materials Chemistry A*
Manuscript ID	TA-ART-07-2020-006813.R1
Article Type:	Paper
Date Submitted by the Author:	13-Aug-2020
Complete List of Authors:	Wilke, Stephen; Northwestern University, Materials Science and Engineering Dunand, David; Northwestern University, Materials Science and Engineering

Fe-Ni Foams Self-Heal during Redox Cycling via Reversible Formation/Homogenization of a Ductile Ni Scaffold

*Stephen K. Wilke, David C. Dunand**

S. K. Wilke, Prof. D. C. Dunand
Department of Materials Science and Engineering
Northwestern University, Evanston, IL, 60208, USA
Email: dunand@northwestern.edu

We investigate the degradation mechanisms during redox cycling of directionally freeze-cast, lamellar Fe foams containing 0, 7, 19, or 25 at. % Ni, relevant to applications in solid-oxide Fe-air batteries and chemical looping processes. In pure Fe, the oxidation/reduction cycle causes a net outward Fe mass flux. This imbalance, left untreated, leads to irreversible microstructural changes: growth of internal microporosity in Fe lamellae and formation of a dense, gas-blocking shell at the foam exterior surface. We propose and demonstrate a novel strategy of alloying Fe with Ni to make reversible the oxidation and reduction pathways, creating a self-healing effect for redox cycling by H_2O/H_2 at 800 °C (representative of a solid-oxide Fe-air battery). During oxidation, each Fe-Ni lamella transforms, *in situ*, into a composite structure with a Ni-rich alloy core and FeO/Fe_3O_4 surfaces. The internal Ni-rich scaffold imparts mechanical stability against oxide fracture and spallation typical of Fe redox materials. During subsequent reduction, the Ni-rich scaffold maintains adhesion to the FeO/Fe_3O_4 surfaces, and Ni catalyzes Fe reduction at the metal/oxide interface. From this interface, Fe diffuses inward to the Ni-rich core, reversing the diffusive flux of the oxidation half-cycle, and Fe-Ni re-homogenization eliminates the microporosity formed within the lamellae during oxidation. Foams are redox-cycled and their microstructural changes are examined by metallography, SEM/EDS, and X-ray diffraction. In pure-Fe

foams, the channel porosity necessary for gas flow decreases from 63 to 27 vol. % after 5 redox cycles, while the deleterious microporosity increases from 3.6 to 13.7% of the lamellae volume. In contrast, Fe-25Ni foams maintain 54 vol. % channel porosity and develop microporosity of only 6.7% of the lamellae volume, with mechanically stable microstructures for at least 20 redox cycles.

1. Introduction

A promising new technology for energy conversion and storage is the solid-oxide Fe-air battery [1–4], a high-temperature device similar to a reversible solid oxide fuel cell (RSOFC). RSOFCs have been proposed for buffering the intermittency of solar and wind power generation, by operating in fuel cell mode when solar and wind production dips, or electrolysis mode when solar and wind provide excess electricity supply [5]. This concept requires large-scale storage of H_2 (and H_2O) used by the RSOFCs, as well as efficient heat recuperation [6]. The solid-oxide Fe-air battery avoids these complications by instead using much smaller volumes of H_2/H_2O to reversibly oxidize Fe and reduce its oxides [1,2], since the redox potentials for Fe/FeO and FeO/Fe_3O_4 are within the range of oxygen partial pressure typical of RSOFC anodes at 550-900 °C [7,8]. Sending the RSOFC exhaust gas directly to the Fe-based redox material in a plug-flow reactor design would be inefficient, due to incomplete gas conversion. Instead, an Fe-air battery is created by filling the RSOFC anode chamber with Fe-based energy storage material (ESM) and hermetically sealing it, with the enclosed H_2/H_2O atmosphere enabling Fe oxidation (battery discharging) and FeO/Fe_3O_4 reduction (battery charging) as the H_2/H_2O composition changes in response to the cell potential, alternating between H_2O- and H_2-rich mixtures, respectively [1,4,9].

As with any secondary battery, two key performance metrics relate to reversibility: (i) reversibility of the oxidation/reduction reactions, to minimize overpotentials and obtain high roundtrip energy efficiency, and (ii) reversibility of redox-induced changes in the active material's microstructure, to maintain consistent storage capacity and rate capability over the battery lifetime. Iron-air batteries face substantial challenges in the latter category: the Fe-based ESM degrades quickly during redox cycling [2,7,10–12]. One degradation path is densification [7,13], driven by sintering and the large molar volume changes

associated with redox (e.g., 114% expansion of Fe to Fe_3O_4), which diminishes the open porosity necessary for H_2/H_2O gas transport. Additions of redox-inactive oxide particles, such as Al_2O_3 [14], TiO_2 [15], ZrO_2 [7], Y_2O_3 [7], and CeO_2 [16], inhibit sintering, but the necessary amount of inactive material (typically > 30 vol. %) drives cost up and energy density down. Battery operation at lower temperatures, 550 or 650 °C [8,17], also decreases degradation effects, while aligning with technological progress in intermediate-temperature SOFCs [18].

The second, thornier, degradation effect is the growth of a gas-blocking exterior shell around the active material [13,19,20], which arises from the irreversible mass flux of Fe inherent to its oxidation and reduction [21]. Iron oxidation is mediated by diffusion of cation vacancies through FeO and Fe_3O_4, since oxygen ion diffusivity is several orders of magnitude smaller than that of iron ions [22,23]. During the oxidation half-cycle, Fe ions diffuse from the interior of the material through the oxide surface layer and react with H_2O at the free surface to form new FeO. This process corresponds to an extreme Kirkendall effect [24–26] – a large imbalance between Fe and O ion interdiffusion – and results in nucleation and growth of Kirkendall micropores at the internal Fe/FeO interface [19]. In contrast, the subsequent reduction half-cycle is a surface-controlled process: Fe islands form on the surface of FeO/Fe_3O_4, and, as they grow, the volume contraction of oxide to metal exposes more oxide for further reaction [27]. There is no driving force during reduction to eliminate the Kirkendall micropores, so with repeated redox cycling the micropores accumulate and Fe mass continues to migrate to the material exterior, which forms the dense gas-blocking shell [19,21]. Shells also form on ESM containing sintering inhibitors [28,29], since the redox-inactive phase addresses densification but not the underlying, irreversible Fe ion mass flux.

Recently, we demonstrated the use of directional freeze-casting to create highly porous (~ 70 vol. %), lamellar Fe foams for use in Fe-air batteries (Figure 1) [13]. Compared to conventional packed powder beds [30] or pellets with random porosity [2], the foam's lamellar structure is designed to prevent sintering, as colonies of parallel Fe lamellae separated by macropore channels can accommodate the large redox volume changes of each individual Fe lamella. Furthermore, the low tortuosity of the long channels is advantageous for gas transport, as compared to powder beds [31,32]. Still, the Kirkendall effect causes a

decrease in channel porosity, since the expansion/contraction of individual lamellae are not reversible: the net outward Fe flux leads to formation of internal microporosity within the lamellae, which make contact with each other thus creating a gas-blocking shell [19]. Iron foams with a dendritic architecture [33,34], rather than lamellar, do not show substantial improvement [35], and while addition of sintering inhibitors such as Y_2O_3-stabilized ZrO_2 has somewhat improved structural stability [29], substantial mechanical stabilization of these foams during redox cycling has so far proved elusive.

Here, we report on a novel approach in improving the structural stability of Fe-based foams as ESM for Fe-air batteries. Aiming to address the irreversibility of redox microstructural changes, we fabricate and test freeze-cast Fe foams alloyed with Ni. Nickel was selected as a promising candidate for alloyed foams because it has a wide solid solution range with Fe, and Ni does not oxidize under Fe-air battery operating conditions [7]. Cobalt also meets these criteria, though Ni was chosen for this investigation due to its lower cost and higher natural abundance. Because Ni remains metallic during the oxidation half-cycle, it forms *in situ* a ductile network throughout the lamellae of the foam, helping to stabilize the FeO/Fe_3O_4 layers. During reduction, freshly reduced Fe rapidly diffuses back into the Ni-rich network, and the re-homogenization process eliminates Kirkendall micropores. The overall result is a cycle of microstructural changes that is self-healing (nearly fully reversible), maintaining the desirable open channels between lamellae and avoiding the growth of micropores within lamellae, thus preventing the gas-blocking shell formation.

The superior mechanical stability of Ni-alloyed Fe foams promises to greatly improve material lifetime and, consequently, retention of capacity and rate capability in solid-oxide Fe-air batteries. Similar high-temperature redox processes, such as chemical looping combustion [36,37] and the steam-iron process [11], could also benefit from this materials design approach applied to operation with different redox gases (e.g., oxidation by air). Recently, Trocino *et al.* [3,38] demonstrated a solid-oxide Fe-air battery in which the ESM is directly joined to the anode, which could eliminate entirely the need for an H_2/H_2O atmosphere. However, one major limitation is that, when iron is oxidized, the electronic conductivity throughout the anode/ESM composite is diminished, so only a fraction of the ESM is utilized. By preserving a

continuous network of metallic Ni even during the oxidation half-cycle, the Fe-Ni foams demonstrated here could enable full utilization of the Fe-air battery design by Trocino *et al*.

2. Experimental

2.1. Fe-Ni foam fabrication

Iron-nickel lamellar foams were prepared via directional freeze casting of an aqueous suspension, freeze drying, and reduction and sintering under flowing H_2 (T_s = 1000 °C, 3.5 h). The fabrication process was the same as detailed in previous work [29], except using suspensions containing submicron α-Fe_2O_3 (99.9%, 325 ± 130 nm, Reade Advanced Materials), nanometric NiO powders (99.5%, 45 ± 15 nm, SkySpring Nanomaterials), polyethylene glycol binder (M_n = 3350, Sigma Aldrich), and Zephrym PD 4974 dispersant (Croda, Inc.). Foams were prepared from suspensions with different ratios of Fe_2O_3:NiO, all with a total of 10 vol. % powder in the suspension (Table S1). These "as-prepared" Fe-Ni foams contained 0, 6.6, 19.0, or 25.0 at. % Ni.

2.2. Redox cycling and characterization

Foams were tested individually using redox conditions simulating the operation of a solid-oxide Fe-air battery at 800 °C, with cyclical oxidation by H_2O and reduction by H_2. Each foam (~0.5 g) was placed on an alumina plate in a tube furnace and heated at 10 °C min^{-1} under 100 sccm flowing H_2. Once equilibrated at 800 °C, the gas was switched to 120 sccm Ar flowed through a 93 °C H_2O bubbler (P^{sat} = 0.78 bar) for 60 min of oxidation. The gas was then switched to 200 sccm H_2 for 90 min of reduction, and these half-cycles were then repeated. After redox cycling was complete, foams were cooled at 10 °C min^{-1} under 100 sccm H_2. For each Fe-Ni composition, three unique foams were tested, each for 5 redox cycles. Additional foams were removed after interrupted cycling (i.e., partway through the first oxidation or reduction) by cooling at 20 °C min^{-1} under 20 sccm 3% H_2 (dry Ar balance) to minimize further redox reactions during cooling. The 60 and 90 min half-cycle durations were selected based on preliminary testing to ensure complete oxidation/reduction reactions between Fe and Fe_3O_4, measured by mass

changes and X-ray diffraction of foams removed after single oxidation or single oxidation/reduction. Foam densification was calculated from diameter and height measurements before and after testing.

After cycling, foams were vacuum-mounted in epoxy (Epothin 2, Buehler) and polished using standard metallographic techniques, with a final vibratory polishing step with 60 nm colloidal silica. In addition to the cycled foams, three as-prepared foams of each composition were mounted and analyzed. Porosity was measured from optical micrographs of cross-sections perpendicular to the freezing direction, at approximately half of the foam height. Since redox structural stability is characterized by retention of desirable channel porosity and avoidance of Kirkendall micropores, images were processed to distinguish between channels (macropores between lamellae) and microporosity (within lamellae) [13].

For porosity calculations, the areal fractions from microscopy images are assumed to accurately represent volume fractions, which is justifiable for perpendicular cross-sections of highly directional, lamellar structures. The total volume of each image (V_{total}) was treated as comprising lamellae (V_{lam}) and channel domains ($V_{channel}$), with the lamellae domain subdivided into solid (V_{sol}) and micropores (V_{micro}). First, a threshold was applied to binarize each image, followed by removal of single pixel outliers to eliminate noise. The channel and micropore domains (i.e., dark pixels) were then analyzed using the BoneJ Thickness algorithm in ImageJ [39], from which $V_{channel}$ and V_{micro} were measured by counting pixels belonging to pores larger and smaller than 4 μm diameter, respectively. Channel- and micro-porosity were calculated by:

$$p_{channel} = \frac{V_{channel}}{V_{total}} \tag{1a}$$

$$p_{micro} = \frac{V_{micro}}{V_{lamellae}} = \frac{V_{micro}}{V_{total} - V_{channel}} \tag{1b}$$

To sample over macrospatial variations in lamellae structure and colony organization, $p_{channel}$ of each foam was calculated from three micrographs covering a total area of 6.0 mm^2 (0.68 μm pixels). To

accurately resolve microporosity, p_{micro} was measured from four higher magnification micrographs per foam (0.51 mm^2 total area, 0.17 μm pixels).

Mounted and polished cross-sections of foams were also analyzed using scanning electron microscopy (Hitachi SU8030) and energy dispersive spectroscopy (SEM/EDS), with an accelerating voltage of 15 kV. The three-dimensional structure of a pure-Fe foam was reconstructed from X-ray computed microtomography (Zeiss Versa 520) using $(1.0\ \mu m)^3$ voxels. The chemical phases of Fe and Fe-25Ni foams were identified using X-ray diffraction (Scintag XDS2000) of mounted foam cross-sections as-prepared, after the first oxidation, and after 5 redox cycles. The X-ray beam sampled a ~5 mm wide strip across the entire cross-section. Phase fractions were calculated using Jade software (Materials Data, Inc.).

2.3. Fe-Ni foils

Fe-Ni foils were prepared and redox-cycled to provide a controlled geometry comparison analogous to the lamellae in Fe-Ni foams. Iron foils 25 μm thick (99.5%, Goodfellow) were cut to approximately 12 × 15 mm and cleaned with acetone, then isopropanol, and dried in air. Nickel was electrodeposited onto the Fe foil strips using a Watts bath [40], pH ~ 3.4, and Ni foil (99+%, Alfa Aesar) counter electrode. The bath was preheated to 50 °C with gentle stirring, and deposition was controlled galvanostatically with a current density of ~20 mA cm^{-2}. After 7 min of electrodeposition, ~4.4 μm of Ni was deposited on each side of the Fe strip, as measured by SEM of mounted and polished cross-sections.

The Fe-Ni bimetallic strip was heated to 1100 °C under flowing 3% H_2 (dry Ar balance) and homogenized for 18 h, with 10 °C min^{-1} heating and cooling rates. The strip was then cut into three pieces, and one piece was used for EDS to confirm full homogenization and measure Ni content. The remaining two pieces (~ 4 × 10 mm) were used for redox cycling, one for a single oxidation and the other for a single oxidation/reduction cycle, using the same experimental procedures as described earlier.

3. Results and Discussion

3.1. Freeze casting of Fe-Ni foams

Iron-nickel foams are prepared by directional freeze casting [41,42] of aqueous suspensions containing submicron Fe_2O_3 and nanometric NiO powders. Following ice sublimation, the Fe_2O_3/NiO green bodies are reduced, homogenized, and sintered under H_2 to obtain Fe-Ni foams with lamellar structures characteristic of ice templating. By varying the ratio of Fe_2O_3:NiO in the suspension (Table S1 in the Electronic Supplementary Information (ESI)), Fe-Ni foams of various compositions are prepared: 0, 6.6, 19, or 25 at. % Ni in the reduced state (referred to as pure-Fe, Fe-7Ni, Fe-19Ni, and Fe-25Ni, respectively). As shown in Figure 1, foams comprise dense lamellae, 8-16 μm in width and spanning several mm in length and height, separated by channels 10-30 μm in width, which are interconnected and open to the foam surface. Each foam consists of several misaligned colonies of lamellae (Figure 1b), originating from separate colonies of ice primary dendrites during freeze casting. Individual Fe-Ni lamellae typically have stubs on one of their two sides (Figure 1c), which are templated from the ice secondary dendrites [43,44].

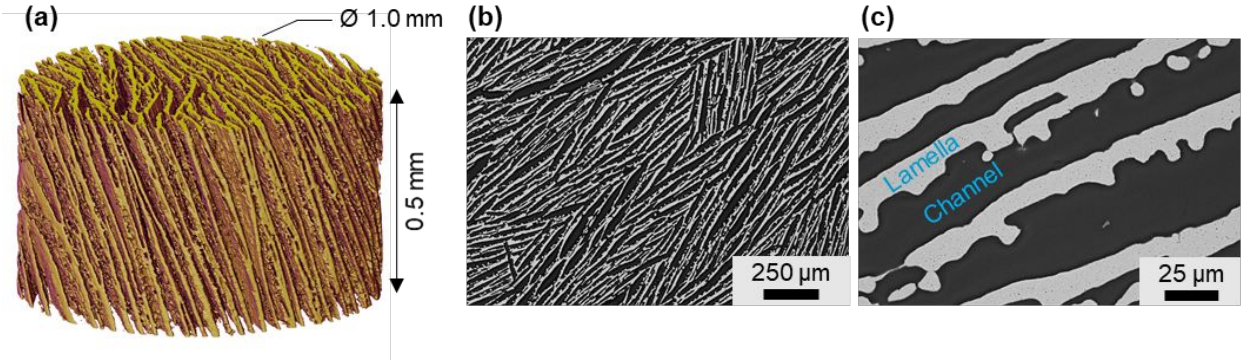

Figure 1. Pure-Fe foam as-prepared via freeze casting of aqueous Fe_2O_3 suspension, followed by reduction and sintering. (a) A partial volume of foam reconstructed from X-ray micro-tomography; (b) optical micrograph of foam cross-section perpendicular to the freezing direction; (c) scanning electron micrograph of same cross-section at higher magnification.

Pure-Fe and Fe-7Ni, -19Ni, and -25Ni foams exhibit comparable initial architectures in terms of channel porosity and size of lamellae and channels (Figure 2a-b). The Ni concentrations of the foams

match the target values for the freeze casting suspensions (Table S1) within ± 0.3 at. %, as measured by energy dispersive spectroscopy (EDS) on several locations throughout the foams. Within individual lamellae, Fe and Ni form a fully homogenous solid solution.

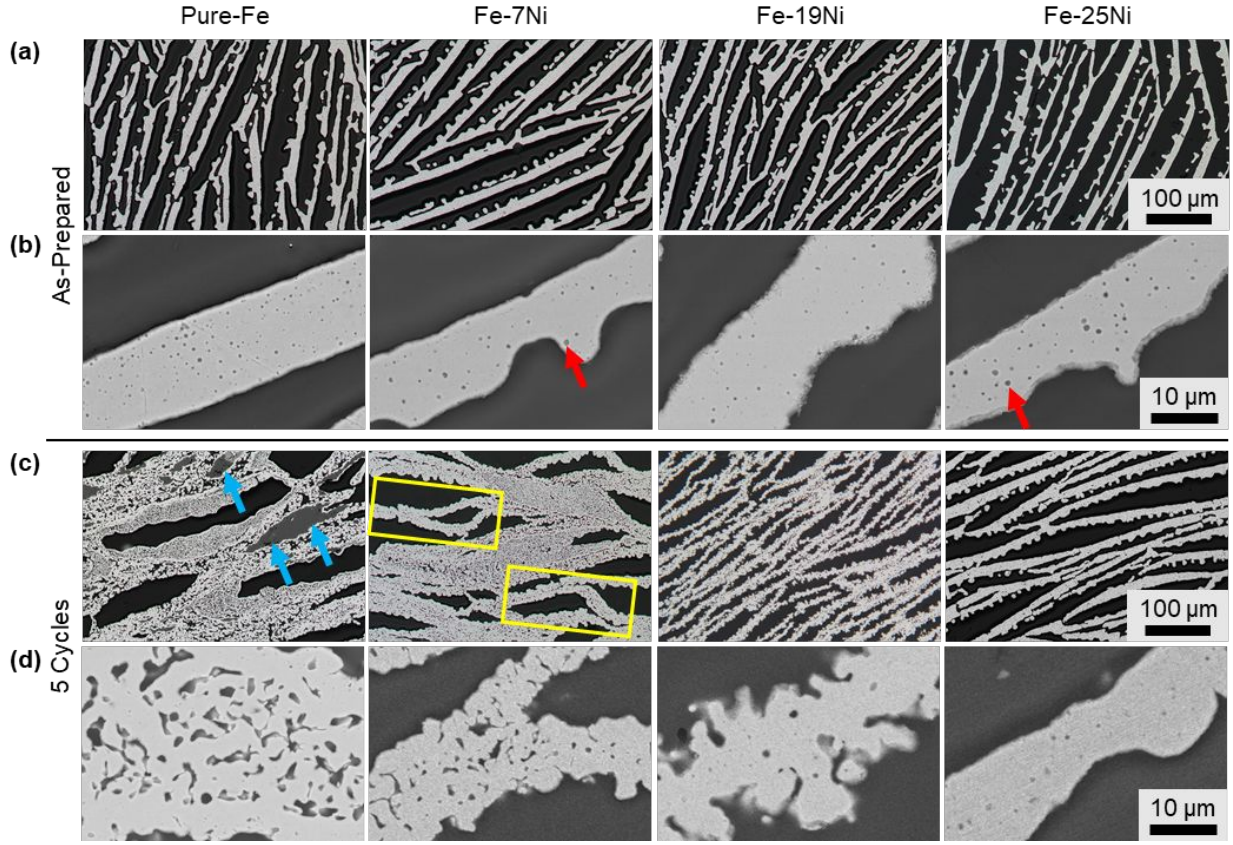

Figure 2. Comparison of structure in pure-Fe and Fe-Ni foams (a-b) as-prepared and (c-d) after 5 redox cycles, showing cross-sections perpendicular to freeze casting direction. As-prepared foams exhibit (a) similar lamellae and channels at low-magnification and (b) minimal microporosity within lamellae (red arrows) at high-magnification. After 5 cycles, increasing Ni content is associated with (c) less constriction of the channels and (d) less microporosity. Annotations mark lamellae buckling (yellow boxes) and residual oxide (blue arrows).

3.2. Foam evolution during redox cycling

3.2.1. Structure and porosity

Since this study focuses on ESM structural evolution, testing of a full Fe-air battery is not necessary. Foam channel porosity, desirable and necessary for gas flow, and lamellae microporosity, deleterious and leading to shell formation, are instead used as indicators for battery performance metrics (e.g., capacity

retention and rate capability). The Fe-Ni foams are redox-cycled under conditions that simulate the full discharge and charge of an Fe-air battery at 800 °C: oxidation by H_2O for 60 min, and reduction by H_2 for 90 min. Based on Fe-Ni-O thermodynamics (discussed later), these reactions result in almost complete Fe conversion between metallic Fe and Fe_3O_4, while Ni remains in a metallic phase. Foams of each composition are individually tested for 5 redox cycles, and their structure and porosity are then compared with as-prepared (i.e., uncycled) foams. Testing on such a small number of cycles is relevant given that (i) 800 °C is a condition of accelerated degradation testing, given recent progress in lowering battery operation temperature to 550-650 °C [8,17,38], and (ii) the most substantial capacity fade and corresponding ESM mechanical degradation occur in the earliest battery cycles.

As shown in Figure 3, all as-prepared foams have similar channel porosity, 62-67% of the total foam volume, regardless of Ni content. All as-prepared foams also show similar microporosity, 1.7-3.6% of the lamellae volume, arising from incomplete sintering of the reduced Fe_2O_3/NiO green bodies (Figure 2b, annotated with red arrows). After 5 redox cycles, however, substantial differences emerge among foams of different Ni content. Consistent with previous work [13], the pure-Fe foams (Fe-0Ni) lose the majority of their desirable channel porosity, decreasing to 27% after 5 cycles. Fe-7Ni behaves similarly to pure-Fe, while Fe-19Ni and Fe-25Ni show significantly enhanced retention of channel porosity. For Fe-25Ni, channel porosity has decreased only to 54 vol. % after 5 cycles, which represents a dramatic stabilization effect of the foam structure compared with pure-Fe. Macroscopic shrinkage of foam diameter, height, and volume upon cycling all decrease with increasing Ni content (Figure S1 in the ESI), indicating less foam densification in agreement with the channel porosity data in Figure 3.

A similarly advantageous trend with increasing Ni content is observed for microporosity after 5 redox cycles (Figure 3): pure-Fe microporosity increases from 3.6 to 13.7% of the lamellae volume, while Fe-25Ni increases to only 6.7%. Since microporosity growth is driven by the irreversibility of the redox microstructural changes, the smaller rise in microporosity for Fe-25Ni again suggests a mechanical stabilization effect imparted by Ni making the structural changes more reversible during redox cycling.

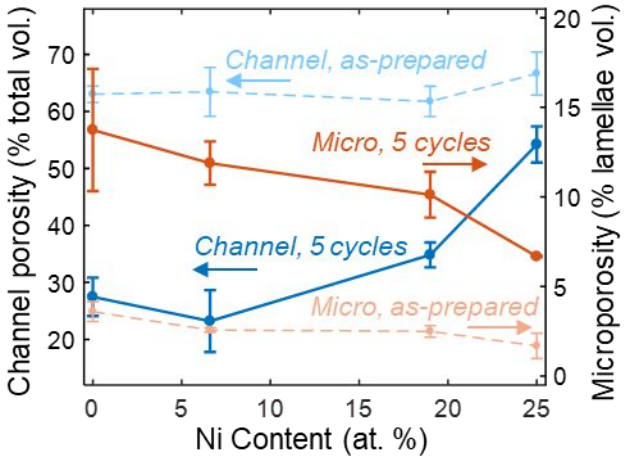

Figure 3. Effect of Ni content on porosity in Fe-Ni foams as-prepared (dashed lines) and after 5 redox cycles (solid lines). Desirable channel porosity (blue markers, left vertical axis) and deleterious microporosity (orange markers, vertical axis) are similar in all as-prepared foams. After 5 cycles, channel porosity is preserved better and microporosity is formed less in foams with higher Ni content. Error bars: ± std. error ($N = 3$).

This trend is clear when comparing micrographs of the foam cross-sections after 5 redox cycles, shown in Figure 2c-d. In addition to changes in channel- and micro-porosity, the pure-Fe and Fe-7Ni foams also show widespread buckling of lamellae (Figure 2c, yellow boxes), evidenced by their undulating morphology compared with the planar lamellae in the as-prepared foams. Lamellae are prone to buckling due to their large geometrical aspect ratio [45,46], and buckling can be triggered by stress associated with spatial variations in redox reaction rates or mechanical constraints, such as an exterior shell [29]. Lamellar buckling also contributes to foam densification by bringing neighboring lamellae into contact, after which they sinter together irreversibly. Another degradation effect caused by channel porosity loss is constriction of gas flow and incomplete utilization of the Fe material, as evidenced in pure-Fe foams by the presence of residual oxide domains (Figure 2c, blue arrows).

In contrast to pure-Fe and Fe-7Ni, the lamellar structure of Fe-19Ni after 5 cycles still resembles the as-prepared foam, albeit with more microporosity and more scalloped surfaces on individual lamellae. Fe-25Ni shows some slight buckling of lamellae, but otherwise the foam structure is nearly unchanged from the as-prepared state. After 10 or 20 redox cycles of Fe-25Ni, the channel porosity, microporosity,

and structure continue to remain stable (Figure 4a-b), suggesting that the Fe-25Ni foam could maintain consistent capacity and rate capability of an Fe-air battery in long-term cycling, especially if operating at lower temperatures where degradation occurs more slowly.

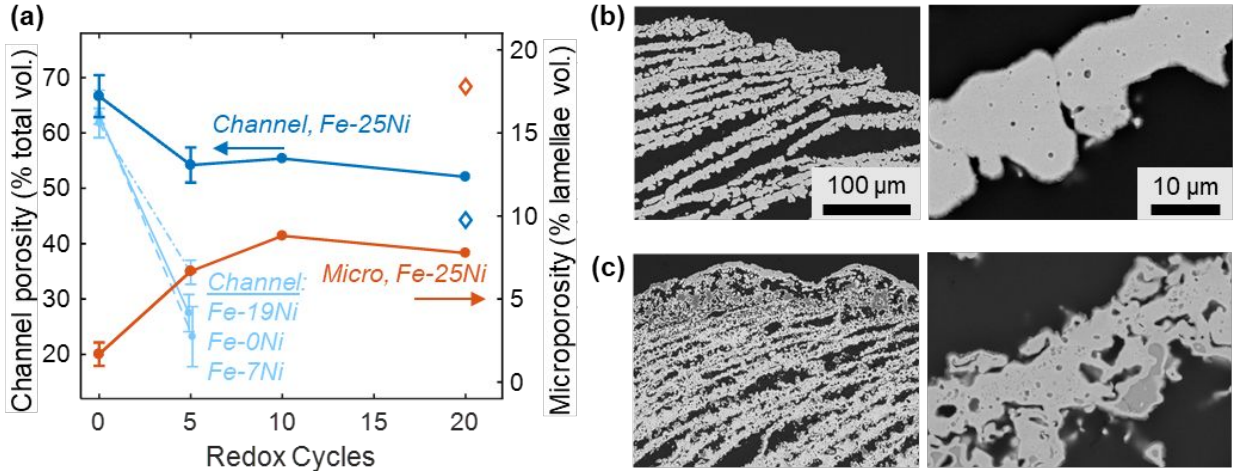

Figure 4. (a) Evolution of porosity in Fe-25Ni foams for up to 20 redox cycles (using 90 min reduction half-cycles), showing desirable channel porosity (blue markers, left vertical axis) and deleterious microporosity (orange markers, right vertical axis); the foam tested for 20 cycles with 10 min reduction half-cycles shown with diamond markers. Channel porosity of other foams after 5 redox cycles shown for reference (light blue). Error bars for 0 and 5 redox cycles: ± std. error ($N = 3$). (b) Fe-25Ni foam cross-sections after 20 redox cycles (90 min reduction half-cycles). (c) Fe-25Ni foam cross-sections after 20 redox cycles (10 min reduction half-cycles) corresponding to diamond markers in (a).

3.2.2 Phase equilibria and transformations

Given the superior reversibility of Fe-25Ni foams, it is important to verify that the Fe-Ni-O thermodynamics are suitable for typical operating conditions of Fe-air batteries or similar redox processes, such as chemical looping combustion. The Fe-Ni-O ternary phase diagram at 800 °C is given in Figure 5a, calculated using Thermo-Calc software, with the initial Fe-Ni foam compositions marked with blue dots. At 800 °C, Fe-Ni alloys forms a γ-FCC solid solution for Ni content > 4 at. %, so the three alloyed foams begin as γ-phase (FCC) and the pure-Fe foam begins as α-phase (BCC). Pure-Fe oxidizes first to FeO and then to Fe_3O_4. For Fe-Ni foams, an example oxidation pathway is marked in Figure 5a with a dashed red arrow for Fe-25Ni. Oxidation begins by formation of FeO (tie line with Fe-25Ni marked in dotted teal), in which Ni has minimal solubility (< 0.51 at. % Ni [47]). The (Fe,Ni) solid solution

286 becomes richer in Ni (purple arrow) as Fe is transformed to FeO. Once the metallic phase reaches 71 at.
287 % Ni, the system enters a three-phase region of Fe-71Ni, FeO, and Fe_3O_4. All FeO is then oxidized to
288 Fe_3O_4 (purple arrow), which is in equilibrium with Fe-71Ni (tie line marked in dashed teal). NiO and
289 Fe_2O_3 do not form under the oxidation conditions here.

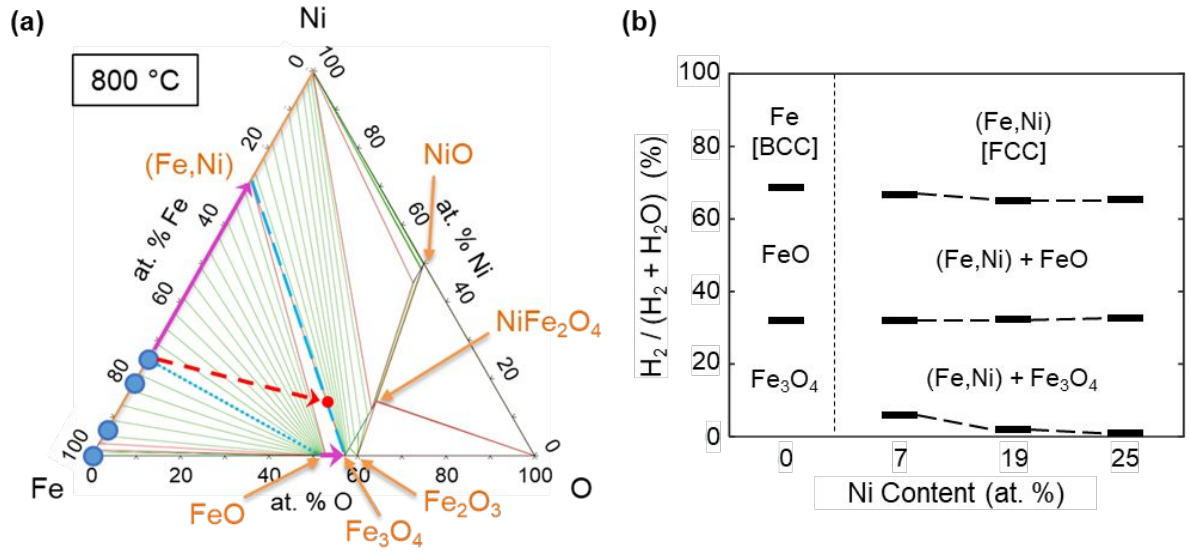

290
291 **Figure 5.** (a) Fe-Ni-O ternary phase diagram, 800 °C isotherm. Annotations mark distinct phases (orange
292 labels), tie lines (green), three-phase regions (light red), initial foam compositions (blue circles), and
293 oxidation pathway for Fe-25Ni: overall trajectory (dashed red arrow) and endpoint (red dot), initial and
294 final tie lines (dotted and dashed teal) with corresponding pathways for the (Fe,Ni) and oxide phases
295 (purple arrows). (b) Equilibrium phases of the Fe-Ni foams in different H_2/H_2O gas mixture compositions
296 at 800 °C [48].
297

298 The oxidation and reduction half-cycle times (60 and 90 min, respectively) were selected to
299 ensure "full" transformation of Fe between the metallic and Fe_3O_4 phases, verified by preliminary testing,
300 in which foams were removed after a single oxidation (1/2 cycle) or a single oxidation/reduction (1
301 cycle). Freeze-cast foams have low specific surface area (~1 $m^2\ g^{-1}$) compared to nanostructured materials
302 common in batteries and fuel cells, so it is important to verify that the test conditions result in complete
303 cycling. After oxidation, XRD patterns of pure-Fe and Fe-25Ni (Figure S2b) show only the Fe_3O_4 phase,
304 and Fe_3O_4 and γ-phases, respectively. Although it is possible for $NiFe_2O_4$ to also form in solid solution
305 with Fe_3O_4 (Figure 5a), this is ruled out by EDS of oxidized Fe-25Ni, which shows Ni is fully absent
306 from the Fe_3O_4 domains. The mass changes upon oxidation of the Fe-7Ni, -19Ni, and -25Ni foams

indicate 96, 92, and 87% of Fe is transformed to Fe_3O_4, respectively, corresponding to final (Fe,Ni) phases with 34, 25, and 28 at. % Fe. These compositions are in close agreement with the tie line between (Fe,Ni) with 29 at. % Fe and Fe_3O_4 (Figure 5a, dashed teal), which is the endpoint for "full oxidation" (red dot, for the Fe-25Ni oxidation pathway). The pure-Fe foam mass change indicates 99% of Fe is oxidized to Fe_3O_4, in agreement with XRD. The foams removed after a single oxidation/reduction show no mass change, indicating full reduction back to metallic (Fe,Ni).

Thus, in the context of an Fe-air battery, switching from pure-Fe to Fe-25Ni decreases the storage material's specific energy density primarily by replacing Fe with non-oxidizing Ni, with an additional slight decrease in the Fe fraction participating in redox. Nickel also introduces much higher materials cost compared to Fe, but nevertheless, Fe-25Ni is a promising advancement given the significant benefits to microstructural stability and material lifetime. Furthermore, the introduction of Ni should not change the battery operating voltage, based on phase equilibria over the pertinent range of oxygen partial pressure (pO_2), or, equivalently, H_2/H_2O mixture compositions (Figure 5b). In an Fe-air battery, the cell potential is determined by the difference in oxygen chemical potential between the anode and cathode (air) according to the Nernst equation. The anode potential corresponds to the phase boundaries of either Fe/FeO ($pO_2 = 7 \times 10^{-20}$ atm, $H_2/(H_2+H_2O) = 69\%$) or FeO/Fe_3O_4 ($pO_2 = 1 \times 10^{-18}$ atm, $H_2/(H_2+H_2O) = 32\%$) [9,49]. As shown in Figure 5b [48], the gas mixture compositions for these phase boundaries are nearly the same for all Fe-Ni compositions, proving that, from a thermodynamic perspective, they are "drop-in" replacements for pure-Fe at 800 °C.

3.3. Mechanisms of redox reversibility and structural stabilization

Understanding the mechanisms by which Ni imparts redox reversibility can guide future research and, more broadly, indicate if the alloying approach is a promising strategy, using other alloying elements. To reveal the role of Ni in the redox process, several pure-Fe and Fe-25Ni foam specimens were removed at various times throughout the first oxidation and reduction.

333 *3.3.1. Oxidation*

334 As explained in the Introduction, the oxidation of pure-Fe lamellae by H_2O occurs via outward Fe
335 diffusion (i.e., inward Fe vacancy diffusion) through the FeO surface layer, leading to nucleation and
336 growth of Kirkendall micropores along the Fe/FeO interface [23,50–52]. Figure 6 shows sequential scanning
337 electron micrographs (SEM) of this process in pure-Fe, illustrating the shrinking Fe core (light gray) and,
338 in the fully oxidized state, lamellae that are split or contain significant microporosity (Figure 6d, red
339 arrows) [19].

340 The evolution of lamellae in Fe-25Ni is quite different, following the oxidation pathway
341 described earlier. Both FeO and Fe_3O_4 form on the lamella surfaces by outward Fe diffusion from the
342 metallic core, which becomes Ni enriched and, in the fully oxidized state, forms a network of Ni-rich
343 alloy within the lamellae cores (Figure 6k, light gray; EDS maps provided in Figure S3). Micrographs of
344 fully oxidized Fe-7Ni and -19Ni lamellae are provided in Figure S4, for comparison. This ductile network
345 surrounded by Fe_3O_4 provides a composite structure much more resistant to bending, buckling, and
346 fracture as compared with Fe_3O_4 alone for the pure-Fe foam. Fe-25Ni also forms much less microporosity
347 (Figure 6k, red arrows), which can be explained by two factors. First, Kirkendall microporosity does not
348 begin forming until the growing FeO reaches some threshold thickness, since Fe vacancies can initially be
349 removed by plastic deformation of FeO via dislocation climb [53–56]. Once FeO becomes thicker, however,
350 its deformation rate slows and vacancies accumulate and precipitate into micropores. Because of the
351 ductile network in the lamella core of Fe-25Ni, the FeO layers do not ever become as thick as in pure-Fe,
352 which may explain the decrease in observed microporosity. Second, Fe vacancies could also be removed
353 via dislocation climb in the metal core, which is present throughout the oxidation of Fe-25Ni lamellae, but
354 shrinks and eventually disappears in pure-Fe, becoming unavailable as a vacancy sink.
355

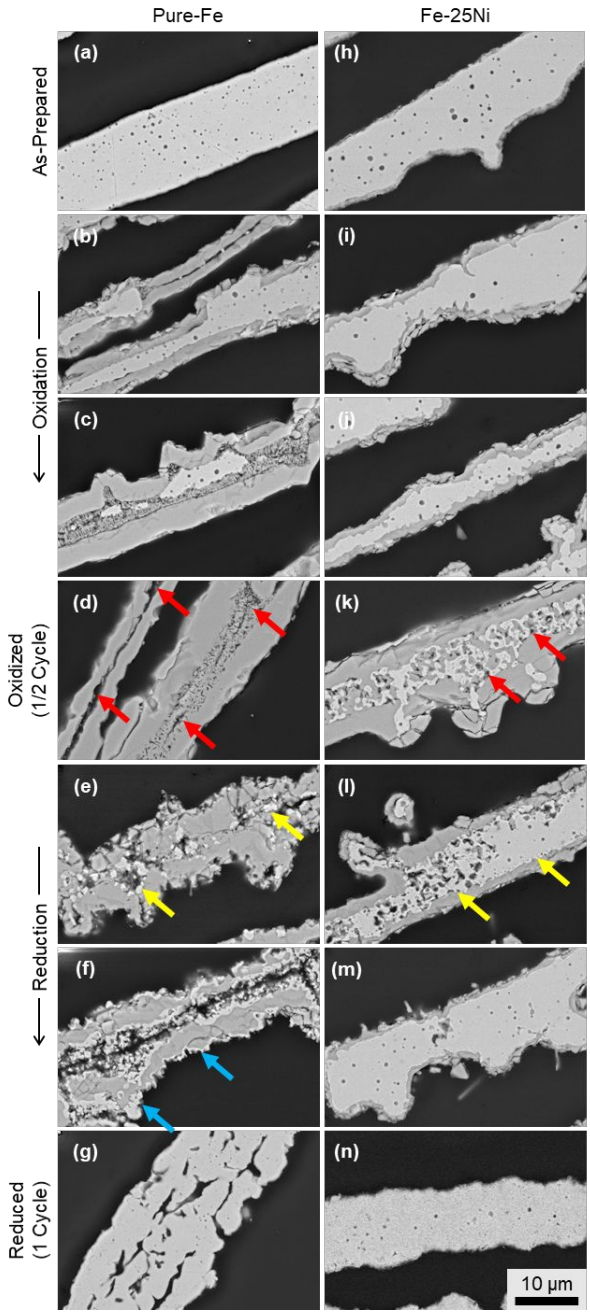

Figure 6. Microstructural evolution of lamellae in (a-g) pure-Fe and (h-n) Fe-25Ni, showing SEM of cross-sections from foams removed at various times throughout the first redox cycle. Metal and oxide phases are light- and dark-gray, respectively; pores are black. Annotations mark Kirkendall micropores and lamellae splitting (red arrows), internal Fe reduction (yellow arrows), and outside surface Fe reduction (blue arrows). (Two lamellae are shown in each (b) and (d); all others show a single lamella.)

This *in situ* formation of a ductile Ni-rich network during oxidation of Fe-Ni alloys by H_2O has also been observed in bimetallic anode catalysts for solid oxide fuel cells (SOFCs) [48] and in Fe-air

batteries [57]. Traditional SOFC anodes use Ni as a catalyst and electronically-conducting phase, but addition of Fe (nearly equiatomic with Ni) has been demonstrated to improve thermal expansion coefficient matching with YSZ, lower the anodic overpotential, and mitigate Ni deactivation [58,59]. Iron is also useful for lowering the device cost for metal-supported SOFCs. Depending on the operating potential, the Fe in these catalysts can be oxidized to FeO/Fe_3O_4 and results in a core-shell microstructure [48] like those observed here, though not intentionally for cycling applications.

3.3.2 Reduction

The reduction process in pure-Fe initiates, unexpectedly, in the interior of individual lamellae, as evidenced by islands of Fe (Figure 6e, yellow arrows). Reduction of the lamella interior requires gas access, which is likely provided by the many fractures and fissures through the FeO/Fe_3O_4 surface layers. Although this access is more restricted than gas reaching the lamellae outside surfaces, a possible explanation is that reduction is kinetically controlled by a surface reaction [27], at least initially [60,61]. Since the interior has very high surface roughness due to the microporosity, the internal reaction rate could initially be higher than that at the smooth outside surface. Shortly into the reduction process, Fe islands do form and grow at the outside surfaces of the lamellae (Figure 6f, blue arrows), but thorough investigation by SEM revealed no locations where reduction on the outside preceded the interior. Fe_3O_4 shrinks in volume as it transforms to FeO and then Fe, and since there is no driving force to eliminate the micropores, the fully reduced lamella still contains significant microporosity (Figure 6g). This microporosity continues to accumulate in later cycles.

In Fe-25Ni, reduction also begins in the lamellae interiors (Figure 6l, yellow arrows) and occurs much more rapidly than in pure-Fe, likely due to the high catalytic activity of Ni and bypassing the step of Fe island nucleation and growth. Reduction of the outer lamellae surfaces is not observed (Figure 6l-m), suggesting that the Ni catalytic effect is sufficiently fast that reduction occurs only at the metal/oxide interface. This difference in reduction mechanism underlies the reversibility that Ni imparts to redox microstructural evolution. The presence of the Ni-rich core maintains adhesion of the FeO/Fe_3O_4 surface

391 layers, preventing fracture and spallation, and as reduction occurs at the metal/oxide interface, the
392 adhesion is never lost. The few Kirkendall micropores that formed during the oxidation half-cycle are also
393 eliminated by re-homogenization of the Fe-Ni alloy, as Fe diffuses back inward from the metal/oxide
394 interface to the core. Since the elemental diffusivities of Fe and Ni are nearly equal in Fe-25Ni [62], no
395 additional Kirkendall microporosity develops during re-homogenization.
396 In pure-Fe, the outward Fe mass flux during oxidation is not reversed during reduction, and the
397 split cores of lamellae are never healed. In contrast, the lamellae in Fe-25Ni are reduced via a pathway
398 that reverses the Fe flux, creating a self-healing effect and returning the lamellae to a fully dense state
399 (Figure 6n).
400
401 *3.3.3 Re-homogenization effects*
402 Complete chemical re-homogenization within individual Fe-Ni lamellae is a crucial step in maintaining
403 reversibility of the microstructural evolution. Qin *et al.* [63] investigated the structural changes in
404 equiatomic FeNi single particles (10-30 μm dia.) after redox cycling via air and H_2 at 700 °C. After 5
405 cycles, these particles exhibited less Kirkendall microporosity than pure-Fe particles, consistent with the
406 results presented here, and the Fe-Ni particles had developed Ni-rich cores and Fe-rich shells. This
407 elemental segregation, without re-homogenization, is reminiscent of the irreversibility of pure-Fe redox
408 materials and will ultimately lead to dense Fe shells that block gas flow. Compared with the redox
409 conditions in this study, several differences in Qin *et al.*'s experiments would make re-homogenization
410 less complete in each redox cycle: lower temperature (700 vs. 800 °C here), larger diffusion lengths (10-
411 30 μm diameter particles vs. 8-16 μm wide lamellae here), shorter reduction time (40 vs. 90 min here),
412 and different oxidation transformations (forming Fe_2O_3 and NiO via oxidation by air vs. forming Fe_3O_4
413 via H_2O here). Still, their observed Fe-Ni segregation is cautionary and merits a closer analysis of the re-
414 homogenization process.
415 Here, the interrupted cycling tests revealed that the entire foam is fully reduced in only 2-10 min
416 (faster for Fe-25Ni than pure-Fe), which is a small fraction of the 90 min half-cycle time. Based on these

observations, an additional Fe-25Ni foam was tested for 20 redox cycles, using only 10 min reduction half-cycles instead of 90 min. The shorter reduction steps provide less time for the re-homogenization process in each cycle, which results in significantly different microstructural changes. After 20 cycles, the Fe-25Ni foam under 90 min reduction half-cycles still exhibits dense lamellae, with only minor shell formation in some areas of the foam exterior (Figure 4b). In contrast, the foam under 10 min reduction half-cycles has developed significant microporosity and a nearly continuous Fe shell (Figure 4c), which contains no Ni according to EDS. This foam has less channel porosity and more microporosity (Figure 4a, diamond markers) compared with the foam under 90 min reduction half-cycles (Figure 4a, circle markers). Thus, the difference in re-homogenization that occurs in a 10 vs. 90 min reduction results in major changes to the microstructural reversibility, suggesting that Fe-Ni does not fully re-homogenize during the shorter reduction time.

The XRD pattern of Fe-25Ni after 5 redox cycles (with 90 min reductions) also indicates incomplete re-homogenization, since it reveals both γ and α phases (Figure S2a). XRD of as-prepared, fully homogenized Fe-25Ni reveals only α-phase at room temperature, due to the martensitic transformation from the γ-phase upon cooling [64]. Higher Ni content in Fe-Ni alloys stabilizes the γ-phase during cooling [65], so the observation that Fe-25Ni after 5 cycles contains both α- and γ-phases at room temperature is consistent with the foam containing, at 800 °C, separate regions that are Ni-poor and Ni-rich. Upon cooling, the former transforms to α-phase and the latter remains stable as γ-phase. The phase compositions predicted from XRD refinement are α-$Fe_{19}Ni_1$ and γ-Fe_3Ni_2 in a 57:43 mixture by weight. Using these values to quantify the degree of homogenization is difficult, however, since at 800 °C the foam contains a continuum of Fe-Ni compositions (i.e., during interdiffusion), which are frozen into the two distinct phases upon cooling. Future work will aim to quantify the re-homogenization kinetics and phase evolution using *in situ* XRD during redox cycling.

Additional information is available in the spatial distributions of Fe, Ni, and O across single lamellae in the interrupted cycling tests, but they are, unfortunately, inconclusive. As shown in Figure S5, EDS line scans across Fe-25Ni lamellae reveal uniform Ni content in the metal phase at all time points

throughout the first redox cycle and even after 20 full cycles (using 90 min reduction half-cycles). This suggests that re-homogenization is rapid compared to the reduction process, which disagrees with previously discussed XRD and microstructural evolution from 10 min reduction half-cycles. It is possible that variations in elemental concentration at small length scales are smoothed out in the EDS line scans due to the electron probe penetration depth (~1 μm).

Finally, re-homogenization data can also be compared with literature on Fe-Ni homogenization rates. The characteristic interdiffusion time can be estimated from the chemical diffusivity – using the average of 5.4×10^{-14} and 7.2×10^{-14} $cm^2\ s^{-1}$ for Fe-20Ni and Fe-30Ni at 800 °C, respectively [66] – and by estimating, from SEM micrographs of a fully oxidized lamella (Figure 6k), a characteristic metal/oxide feature size of ~1 μm. For bulk diffusion in 3D, these values yield a characteristic time, $t_c = l_c^2/6D$ = 7.4 h, which is ~5 × longer than the reduction half-cycle time of 1.5 h. However, two other factors likely contribute to faster interdiffusion than the t_c estimate. First, during oxidation, the metallic phase may act as a vacancy sink via its plastic deformation (dislocation climb). If this occurs, the Ni-rich phase will have large plastic strain when reduction begins, which could be relieved by its recrystallization into fine grains. Additional vacancy diffusion via grain boundaries would shorten the re-homogenization time compared to the characteristic time predicted from bulk values for diffusivity. Second, the re-homogenization process may be accelerated by the presence of volatile $Ni(OH)_2$, whose vapor pressure increases with H_2O content in H_2/H_2O gas atmospheres [67]: in SOFC Ni/YSZ anodes, one of the dominant mechanisms of Ni catalyst coarsening is gas-phase migration of $Ni(OH)_2$ [68–70]. During reduction of Fe-25Ni lamellae, the local gas environment near the metal/oxide reduction sites could range between 0 and 67% H_2O (Figure 5b), so $Ni(OH)_2$ could be increasing surface diffusion rates.

In summary, full re-homogenization of Fe-Ni during each reduction half-cycle is a necessary condition for self-healing, reversible redox microstructural changes. Collectively, the data available from XRD, EDS, literature diffusivity data, and microstructural changes resulting from different reduction half-cycle times all indicate that 90 min is near the threshold for sufficient reduction and re-homogenization

time in these Fe-25Ni foams. Reduction durations longer than 90 min may further improve foam structural reversibility. From an application standpoint, this will likely not be a critical issue for Fe-air batteries installed for grid-tied energy storage, where duty cycles are often partial charge/discharge spanning several hours, rather than continuous, full capacity cycling. The material could also be periodically rejuvenated by short treatments at 900 °C to accelerate full homogenization, which should not incur substantial sintering since the foams were initially sintered at 1000 °C.

3.4. Redox cycling of Fe-Ni foils

In addition to testing Fe-Ni foams, Fe-Ni foils were redox cycled to provide a comparison using a simplified geometry similar to an individual lamella. These Fe-Ni foils (~ 4 × 10 mm) were prepared by electrodepositing Ni onto 25 μm thick Fe foils, followed by homogenization at 1100 °C for 18 h. These foils are dense after homogenization (no Kirkendall micropores), again due to the nearly equal diffusivities of Fe and Ni [62]. The foil composition most closely matching the foams was Fe-27Ni, measured by EDS. The microstructures of pure-Fe and Fe-27Ni foils are compared in Figure 7 in the as-prepared state, after first oxidation (1/2 cycle), and after the first reduction (1 cycle). Microstructural changes in pure-Fe foil are qualitatively similar to those in the foam lamellae: the initially dense foil develops Kirkendall microporosity and a central void during oxidation (Figure 7, red arrows), and the microporosity remains after reduction.

Fe-27Ni foil, however, evolves differently than lamellae in Fe-25Ni foam. During oxidation, Fe-27Ni develops a Ni-rich network in the foil core, but the adhesion between the metallic core and surface Fe_3O_4 layers is poor, corresponding to an accumulation of Kirkendall micropores at the metal/Fe_3O_4 interface (Figure 7, red arrows). Consequently, one of the Fe_3O_4 layers delaminated from the foil during metallographic mounting (yellow box). Upon reduction, the interfacial microporosity prevents re-homogenization, and the core and surface layers are reduced separately. Since the core is Ni-rich, its volumetric shrinkage is much less than the surface layers, so adhesion is completely lost and the surface layers delaminate. Nickel resides only in the core layer after reduction, as measured by EDS.

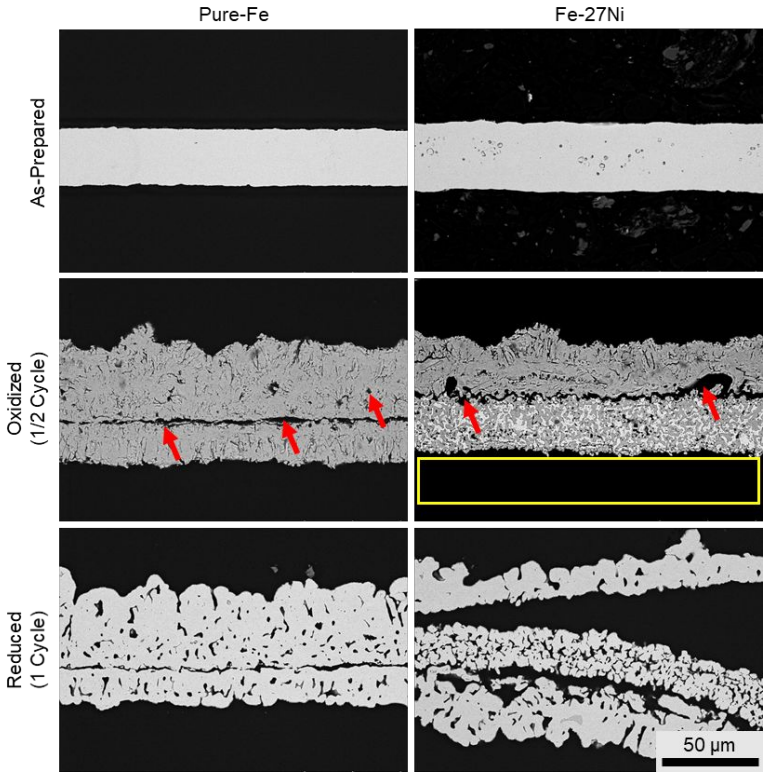

Figure 7. Microstructural evolution of pure-Fe and Fe-27Ni foils. SEM of foil cross-sections as-prepared, oxidized (1/2 cycle), and reduced (1 cycle). Metal and oxide phases are light- and dark-gray, respectively; pores are black. Annotations mark Kirkendall micropores and lamellae splitting (red arrows), and missing oxide layer delaminated during metallographic mounting (yellow box).

The Fe-27Ni foil does not exhibit self-healing due to the larger amount of microporosity at the metal/oxide interface, as compared with the Fe-25Ni foam lamellae. One explanation for this difference is a size effect, similar to that reported for the NiTi system: nickel wires coated with titanium develop increasing amounts of internal microporosity upon Ni-Ti interdiffusion (at 925 °C) as the initial wire size increases (25, 50, 100 µm dia.), due to a strong Kirkendall effect in the Ni_3Ti phase [71]. For our foams, fewer Kirkendall micropores develop for thinner oxide layers, so the larger initial thickness of Fe-27Ni foil (34 µm, vs. 8-16 µm thick foam lamellae) may be responsible for its poorer redox structural stability. There may exist an optimum range for characteristic size (e.g. particle diameter, lamella thickness) in Fe-25Ni redox materials. As seen with the foil, materials that are too thick are still prone to Kirkendall microporosity, disrupting adhesion between the ductile metal core and surface oxide layers during

oxidation. Materials that are too thin, on the other hand, are more susceptible to sintering or, in the case of freeze-cast foams, buckling that leads to contact and sintering between neighboring lamellae [13].

4. Conclusions

High-temperature Fe-based redox materials, such as those for Fe-air batteries or chemical looping combustion, degrade due to sintering, large volumetric changes, and irreversible Fe mass flux arising from the disparate mechanistic pathways of Fe oxidation and reduction. We address the latter problem by creating Fe-Ni foams via directional freeze casting and demonstrating the superior reversibility of their microstructural evolution during oxidation/reduction cycling via H_2O and H_2 at 800 °C. The highly porous (62-67 vol. %), lamellar architecture of these foams also accommodates the large redox volume changes and resists sintering, making them mechanically robust. For up to 25 at. % Ni, Fe-Ni is a drop-in replacement for Fe-air batteries and will not affect cell voltage, based on phase equilibria in H_2/H_2O atmospheres.

The addition of Ni, specifically in Fe-25Ni foams, introduces several changes to the redox process that impart structural redox reversibility via a self-healing effect, as summarized in Figure 8:

1. In the fully oxidized state of the foam, Ni remains metallic and forms a continuous, ductile network within the individual lamellae of the foam. The composite structure – Ni-rich metal core and Fe_3O_4 surface layers – is more mechanically resistant to buckling and fracture as compared to only Fe_3O_4, in the case of pure-Fe foams.
2. Less Kirkendall microporosity forms during oxidation of Fe-25Ni as compared to pure-Fe, diminishing the irreversible widening of lamellae and constriction of channel pores.
3. Adhesion between the Ni-rich metal core and surface FeO/Fe_3O_4 layers is maintained throughout each redox cycle, preventing irreversible fracture and delamination as observed in pure-Fe lamellae.

4. During reduction, Fe-Ni re-homogenizes as Fe diffuses inward to the Ni-rich core, reversing the outward Fe flux of the oxidation half-cycle, thereby eliminating Kirkendall micropores and returning the lamella to a nearly fully dense state.

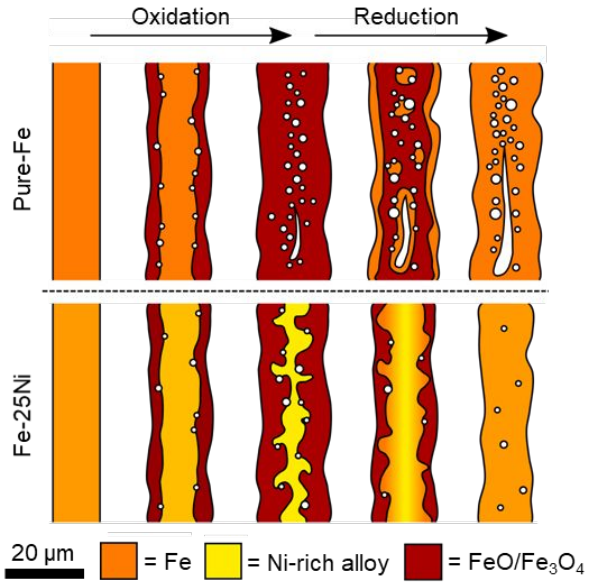

Figure 8. Summary schematic of microstructural evolution in single lamellae of pure-Fe and Fe-25Ni foams. Scale bar is approximate (lamellae begin 8-16 µm thick).

In Fe-25Ni foams, the channel porosity necessary for gas flow remains stable (≥ 52-54 vol. %), and the microporosity within lamellae associated with gas-blocking shell formation is avoided, as demonstrated for up to 20 redox cycles. However, the reduction half-cycle must be allotted sufficient time for Fe-Ni to re-homogenize (~90 min for these foams and test conditions), or the degradation effects typical of pure-Fe also occur in Fe-Ni, as Fe becomes increasingly segregated to the surfaces of lamellae and the foam exterior, sealing it off to gas exchange by forming a solid shell.

Alloying of Fe redox materials with Ni demonstrates a new route to improve the reversibility of microstructural changes during redox cycling. More broadly, the reversibility observed in Fe-25Ni suggests that the alloying approach may hold promise using other, unexplored alloying elements to address long-standing problems with redox material lifetime.

Acknowledgements

This work was supported by the National Science Foundation (NSF CMMI-1562941). Experiments and characterization made use of several Northwestern University resources: the Materials Characterization and Imaging Facility, the NUANCE Center (supported by SHyNE under NSF ECCS-1542205, MRSEC under NSF DMR-1720139, the International Institute for Nanotechnology, the Keck Foundation, and the State of Illinois), and the Jerome B. Cohen X-Ray Diffraction Facility (also supported by MRSEC and SHyNE). X-ray microtomography data were acquired at the U.S. Naval Research Laboratory by Dr. Andrew Geltmacher.

The authors gratefully acknowledge the following researchers at Northwestern University: Mr. Connor Carr for assistance in Ni electrodeposition on Fe foils (with use of equipment in the laboratories of Prof. Sossina Haile), as well as Dr. Christoph Kenel, Dr. Alexander Chadwick, Ms. Kristen Scotti, and Mr. Chuan Liu for insightful discussions.

Additional Information

Electronic Supplementary Information (ESI) accompanies this paper online.

Conflict of interest

DCD discloses a financial interest in Cell Mobility, Inc., a company involved with metal foams.

References

1 N. Xu, X. Li, X. Zhao, J. B. Goodenough and K. Huang, *Energy Environ. Sci.*, 2011, **4**, 4942.

2 A. Leonide, W. Drenckhahn, H. Greiner and H. Landes, *J. Electrochem. Soc.*, 2014, **161**, A1297–A1301.

3 S. Trocino, S. C. Zignani, M. Lo Faro, V. Antonucci and A. S. Aricò, *Energy Technol.*, 2017, **5**, 670–680.

4 A. Inoishi, T. Sakai, Y. W. Ju, S. Ida and T. Ishihara, *J. Power Sources*, 2014, **262**, 310–315.

5 C. Graves, S. D. Ebbesen, S. H. Jensen, S. B. Simonsen and M. B. Mogensen, *Nat. Mater.*, 2015, **14**, 239–244.

6 S. H. Jensen, C. Graves, M. Mogensen, C. Wendel, R. Braun, G. Hughes, Z. Gao and S. A. Barnett, *Energy Environ. Sci.*, 2015, **8**, 2471–2479.

7 C. M. Berger, O. Tokariev, P. Orzessek, A. Hospach, Q. Fang, M. Bram, W. J. Quadakkers, N. H. Menzler and H. P. Buchkremer, *J. Energy Storage*, 2015, **1**, 54–64.

8 X. Zhao, Y. Gong, X. Li, N. Xu and K. Huang, *J. Electrochem. Soc.*, 2013, **160**, A1716–A1719.

9 Q. Fang, C. M. Berger, N. H. Menzler, M. Bram and L. Blum, *J. Power Sources*, 2016, **336**, 91–98.

10 N. H. Menzler, A. Hospach, L. Niewolak, M. Bram, O. Tokariev, C. Berger, P. Orzessek, W. J. Quadakkers, Q. Fang and H. P. Buchkremer, *ECS Trans.*, 2013, **57**, 255–267.

11 A. Thursfield, A. Murugan, R. Franca and I. S. Metcalfe, *Energy Environ. Sci.*, 2012, **5**, 7421–7459.

12 Y. Saito, F. Kosaka, N. Kikuchi, H. Hatano and J. Otomo, *Ind. Eng. Chem. Res.*, 2018, **57**, 5529–5538.

13 S. K. Wilke and D. C. Dunand, *Acta Mater.*, 2019, **162**, 90–102.

14 A. M. Kierzkowska, C. D. Bohn, S. A. Scott, J. P. Cleeton, J. S. Dennis and C. R. Müller, *Ind. Eng. Chem. Res.*, 2010, **49**, 5383–5391.

15 B. M. Corbella and J. M. Palacios, *Fuel*, 2007, **86**, 113–122.

16 X. Zhu, M. Zhang, K. Li, Y. Wei, Y. Zheng, J. Hu and H. Wang, *Chem. Eng. Sci.*, 2018, **179**, 92–103.

17 X. Zhao, Y. Gong, X. Li, N. Xu and K. Huang, *J. Electrochem. Soc.*, 2013, **160**, A1241-1247.

18 D. J. L. Brett, A. Atkinson, N. P. Brandon and S. J. Skinner, *Chem. Soc. Rev.*, 2008, **37**, 1568–1578.

19 S. K. Wilke and D. C. Dunand, *J. Power Sources*, 2020, **448**, 227463.

20 C. Zhang, C. Ji, W. Wang, D. Schmidt, X. Jin, J. P. Lemmon and K. Huang, *Energy Environ. Sci.*,

2016, **9**, 3746–3753.

21 D. Neagu, E. I. Papaioannou, B. Tjaden, X. Lu, C. Mak, M. W. Gaultois, B. Ray, P. Shearing and I. S. Metcalfe, *Sci. Rep.*, 2020, **10**, 5266.

22 W. K. Chen and N. L. Peterson, *J. Phys. Chem. Solids*, 1975, **36**, 1097–1103.

23 R. Bredesen and P. Kofstad, *Oxid. Met.*, 1991, **35**, 107–137.

24 H. J. Fan, U. Gösele and M. Zacharias, *Small*, 2007, **3**, 1660–1671.

25 Y. Yin, R. M. Rioux, C. K. Erdonmez, S. Hughes, G. A. Somorjai, A. P. Alivisatos, C. Chen and K. N. Tu, *Science*, 2004, **304**, 711–4.

26 A. A. El Mel, P. Y. Tessier, M. Buffiere, E. Gautron, J. Ding, K. Du, C. H. Choi, S. Konstantinidis, R. Snyders, C. Bittencourt and L. Molina-Luna, *Small*, 2016, **12**, 2885–2892.

27 Q. Jeangros, T. W. Hansen, J. B. Wagner, C. D. Damsgaard, R. E. Dunin-Borkowski, C. Hébert, J. Van Herle and A. Hessler-Wyser, *J. Mater. Sci.*, 2013, **48**, 2893–2907.

28 Z. Sun, Q. Zhou and L. S. Fan, *Langmuir*, 2013, **29**, 12520–12529.

29 S. K. Wilke, R. A. Lundberg and D. C. Dunand, *ACS Appl. Mater. Interfaces*, 2020, **12**, 27190–27201.

30 X. Zhao, X. Li, Y. Gong and K. Huang, *Chem. Commun.*, 2014, **50**, 623–625.

31 A. Z. Lichtner, D. Jauffrès, D. Roussel, F. Charlot, C. L. Martin and R. K. Bordia, *J. Eur. Ceram. Soc.*, 2015, **35**, 585–595.

32 J. Seuba, S. Deville, C. Guizard and A. J. Stevenson, *Sci. Technol. Adv. Mater.*, 2016, **17**, 313–323.

33 H. Park, T. Um, K. Hong, J. S. Kang, H.-S. Nam, K. Kwon, Y.-E. Sung and H. Choe, *Metall. Mater. Trans. B*, 2018, **49**, 2182–2190.

34 R. Sepúlveda, A. A. Plunk and D. C. Dunand, *Mater. Lett.*, 2015, **142**, 56–59.

35 T. Um, S. K. Wilke, H. Choe and D. C. Dunand, *J. Alloys Compd.*, 2020, 156278.

36 A. Mishra and F. Li, *Curr. Opin. Chem. Eng.*, 2018, **20**, 143–150.

37 M. M. Hossain and H. I. de Lasa, *Chem. Eng. Sci.*, 2008, **63**, 4433–4451.

38 S. Trocino, M. Lo Faro, S. C. Zignani, V. Antonucci and A. S. Aricò, *Appl. Energy*, 2019, **233–234**, 386–394.

39 R. P. Dougherty and K.-H. Kunzelmann, *Microsc. Microanal.*, 2007, **13**, 1678–1679.

40 Nickel Institute, *Nickel Plating Handbook*, 2013.

41 K. L. Scotti and D. C. Dunand, *Prog. Mater. Sci.*, 2018, **94**, 243–305.

42 S. Deville, *Freezing Colloids: Observations, Principles, Control, and Use*, Springer, Cham, Switzerland, 2017.

43 S. Deville, E. Saiz, R. K. Nalla and A. P. Tomsia, *Science*, 2006, **311**, 515–518.

44 C. Pekor, B. Groth and I. Nettleship, *J. Am. Ceram. Soc.*, 2010, **93**, 115–120.

45 M. M. Porter, R. Imperio, M. Wen, M. A. Meyers and J. McKittrick, *Adv. Funct. Mater.*, 2014, **24**, 1978–1987.

46 A. Ojuva, M. Järveläinen, M. Bauer, L. Keskinen, M. Valkonen, F. Akhtar, E. Levänen and L. Bergström, *J. Eur. Ceram. Soc.*, 2015, **35**, 2607–2618.

47 A. D. Dalvi and W. W. Smeltzer, *J. Electrochem. Soc.*, 1970, **117**, 1431–1436.

48 N. Xu, M. Chen and M. Han, *J. Alloys Compd.*, 2018, **765**, 757–763.

49 X. Zhao, N. Xu, X. Li, Y. Gong and K. Huang, *RSC Adv.*, 2012, **2**, 10163–10166.

50 H. J. Engell, *Acta Metall.*, 1958, **6**, 439–445.

51 W. W. Smeltzer, *Acta Metall.*, 1960, **8**, 377–383.

52 D. J. Young and H. Yin, *Oxid. Met.*, 2013, **79**, 445–460.

53 J. D. Mackenzie and C. E. Birchenall, *Corrosion*, 1957, **13**, 17–19.

54 Y. Hidaka, T. Anraku and N. Otsuka, *Oxid. Met.*, 2003, **59**, 97–113.

55 A. G. Evans, D. Rajdev and D. L. Douglassw, *Oxid. Met.*, 1972, **4**, 151–170.

56 A. G. Evans, D. R. Mumm and J. W. Hutchinson, *Prog. Mater. Sci.*, 2001, **46**, 505–553.

57 T. Sakai, A. Inoishi, M. Ogushi, S. Ida and T. Ishihara, *J. Energy Storage*, 2016, **7**, 115–120.

58 T. Ishihara, J. Yan, M. Shinagawa and H. Matsumoto, *Electrochim. Acta*, 2006, **52**, 1645–1650.

59 H. C. Park and A. V Virkar, *J. Power Sources*, 2009, **186**, 133–137.

60 K. Piotrowski, K. Mondal, H. Lorethova, L. Stonawski, T. Szymański and T. Wiltowski, *Int. J. Hydrogen Energy*, 2005, **30**, 1543–1554.

61 Y. D. Wang, X. N. Hua, C. C. Zhao, T. T. Fu, W. Li and W. Wang, *Int. J. Hydrogen Energy*, 2017, **42**, 5667–5675.

62 C. E. Campbell, *Diffusivity and Mobility Data, ASM Handbook, Volume 22A: Fundamentals of Modeling for Metals Processing*, 2009.

63 L. Qin, A. Majumder, J. A. Fan, D. Kopechek and L.-S. Fan, *J. Mater. Chem. A*, 2014, **2**, 17511–17520.

64 G. Cacciamani, A. Dinsdale, M. Palumbo and A. Pasturel, *Intermetallics*, 2010, **18**, 1148–1162.

65 A. L. Schaeffler, *Met. Prog.*, 1949, **56**, 680.

66 E. A. Brandes and G. B. Brook, Eds., *Smithells Metals Reference Book*, 7th edn., 1992.

67 L. Holzer, B. Iwanschitz, T. Hocker, B. Münch, M. Prestat and D. Wiedenmann, *J. Power Sources*, 2011, **196**, 1279–1294.

68 D. Simwonis, F. Tietz and D. Stover, *Solid State Ionics*, 2000, **132**, 241–251.

69 E. Lay-grindler, J. Laurencin, J. Villanova, P. Cloetens, P. Bleuet and A. Mansuy, *J. Power Sources*, 2014, **269**, 927–936.

70 Z. Jiao, N. Takagi, N. Shikazono and N. Kasagi, *J. Power Sources*, 2011, **196**, 1019–1029.

71 A. R. Yost, D. Erdeniz, A. E. Paz and D. C. Dunand, *Intermetallics*, 2019, **104**, 124–132.

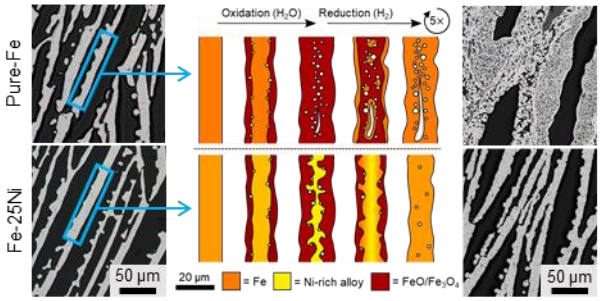

Alloying Fe foams with Ni creates a self-healing effect of lamellar structure for extended high-temperature redox cycling via H_2/H_2O.